N69- 40950
NASA CR- 106456

METHOD FOR ESTIMATING THE ELECTRICAL CONDUCTIVITY OF THE LUNAR INTERIOR

September 22, 1969

Bellcomm, Inc.

BELLCOMM, INC. TR-69-103-7-4

METHOD FOR ESTIMATING THE ELECTRICAL CONDUCTIVITY OF THE LUNAR INTERIOR

September 22, 1969

W. R. Sill
J. L. Blank

Work performed for Manned Space Flight, National Aeronautics and Space Administration under Contract NASW-417.

TR-69-103-7-4

ABSTRACT

A theoretical investigation of the lunar interaction with the solar wind and its electric and magnetic fields reveals a method for estimating the electrical conductivity of the lunar interior. Data from a single lunar surface magnetometer, in conjunction with simultaneous measurements of the interplanetary magnetic field and solar wind velocity, should provide sufficient information to distinguish between various classes of conductivity models. Such models are based on different thermal histories and assumed lunar materials.

TABLE OF CONTENTS

METHOD FOR ESTIMATING THE ELECTRICAL CONDUCTIVITY OF THE LUNAR INTERIOR

1. INTRODUCTION

Since the electrical conductivity of the moon determines the strength of the induced magnetic field, the study of the interaction of the moon with the solar wind and the interplanetary electromagnetic field offers an attractive method for estimating the lunar conductivity profile. In fact, the observed absence of a strong disturbance in the solar wind on the sunlit side of the moon implies that the energy density of any lunar magnetic field is much less than that of the streaming solar wind, and this bound, in turn, places certain restrictions on permissible lunar conductivity models.

The induced lunar magnetic field arises in response to two sources, the motional solar wind electric field and the time rate of change of the interplanetary magnetic field. The observation that the solar wind-moon interaction is weak implies that essentially the entire undisturbed solar wind electric and magnetic fields are available to drive induction currents. In response to the motional electric field, currents flow through the moon and close in the solar wind, whereas the time-varying magnetic source drives eddy currents which close in the lunar interior. This basic difference in the current flow pattern in response to the two sources allows a simple exposition of the dependence of the induced fields on various conductivity structures. Consider for example a layered sphere with conductivity increasing with lunar depth. Currents driven by the interplanetary electric field cross layer interfaces, and the resistances of the layers add in series. Any layer which represents a very high resistance in the current path will tend to limit the current and the corresponding magnetic field. On the other hand, the current flow induced by the interplanetary magnetic field is parallel to the layer interfaces, and the layer resistances add in parallel. Here the layer with the lowest resistance will be most influential in determining the strength of the induced field.

The response driven by the time-varying magnetic source was studied by Blank and Sill [1969a, hereafter referred to as Paper I] and Sill and Blank [1968] who show that the induced magnetic field is poloidal (radial and tangential components). The induced field in this mode becomes important at frequencies where induction takes place in the most conductive portion of the moon, the interior.

The response to the motional electric field was studied first in the DC limit [see e.g., Sonett and Colburn, 1967]. This interaction gives rise to a toroidal induced magnetic field (tangential component only) whose magnitude depends on the total resistance to the current flow across the moon. The extension of the study of the toroidal mode to account for time variations in the motional field is presented by Blank and Sill [1969b] who show that, for a core-crust model at the frequencies of interest here, the response is frequency independent and equal to the DC response. For the case where the crust resistance is much less than the core resistance, the condition that no strong interaction take place (magnetic energy density much less than solar wind energy density; $B^2/2\mu << nmV^2$) requires that the core conductivity be less than 10^{-5} $(\Omega m)^{-1}$ [Hollweg, 1968], a condition essentially the same as that for an assumed homogeneous moon. On the other hand, when the crust resistance dominates, one finds that the condition for no strong interaction is $\sigma_s < 10^{-11} z$, where σ_s is the conductivity of a surface layer of thickness z in meters [Hollweg, 1968]. Thus a conductive core enveloped by a surface layer of 100m to 1 km of dry rock $(\sigma < 10^{-9} (\Omega m)^{-1})$ or even a 10m layer of very resistive rock or debris $(\sigma < 10^{-10} (\Omega m)^{-1})$ would be compatible with the absence of a strong interaction.

Recently Ness [1969a, 1969b] has attributed interplanetary field reversal transients observed in the lunar wake to induction effects in the lunar interior. He thereby estimates the lunar Cowling time to be ∿20 sec, which corresponds to an interior lunar conductivity of $\sim 10^{-4}$ $(\Omega m)^{-1}$. However, since the field perturbations observed in the wake are primarily caused by diamagnetic plasma currents in the wake penumbra, it might be questioned whether the transient effects observed are indeed due to induction in the moon. But even if the transient effects are attributable to lunar induction, the observed Cowling time is compatible with either a poorly conductive lunar interior $(\sigma \sim 10^{-4} (\Omega m)^{-1})$ or a conductive interior shielded by a poorly conductive crust, in which case the observed transient is due to the decay of the toroidal mode.

Thus the interpretations of observations made from lunar orbit are compatible with either a poorly conductive lunar interior or a conductive interior enveloped by a very resistive crust. To determine the conductivity of the lunar interior it will probably be necessary to utilize magnetic field measurements made on the surface. The purpose of this paper is to describe an experiment, based in part on the theory of Paper I, in which measurements of the lunar surface magnetic field, such as those anticipated from the Apollo Lunar Surface Experiments Package (ALSEP) magnetometer, can be used to estimate the interior electrical conductivity. Our preliminary investigations indicate that the resolution of this experimental method should be sufficient to distinguish between various classes of proposed conductivity profiles.

We begin with a discussion of the interplanetary magnetic and electric source fields, which are the input driving forces in the theory, and a brief discussion of lunar conductivity models. An analysis of multi-layer models follows, which applies the surface current model of Paper I to the experiment. Computational results are then presented and general conclusions regarding the objective and limitations of the experiment are drawn. It is found that, within the frequency range ($3x10^{-6}$Hz $< f <10^{-3}$Hz) imposed by the theory and experimental constraints, the toroidal response is frequency independent and its magnitude depends strongly on the surface conductivity structure for most reasonable models. However, in this frequency range the poloidal response for the hot and cold models of England et al. [1968] is frequency dependent, and thus the poloidal response may provide information on the interior electrical structure.

2. INTERPLANETARY MAGNETIC AND ELECTRIC FIELDS

There exist fluctuations in the interplanetary magnetic field due to many sources, e.g., waves and turbulence. We are principally concerned with those fluctuations caused by solar wind convection of large scale spatial inhomogeneities in the interplanetary field. For example, the power density spectrum at the lower frequencies is dominated by the apparent corotation of the sector structure with the sun. Simultaneous measurements of the magnetic field by two spacecraft separated by 1.3×10^6 km show a high degree of correlation, with a time lag corresponding to the time necessary to rotate the field pattern from one observation point to the other [Ness, 1966]. Thus at least for separations $\lesssim 10^6$ km, measurements at one point may be used to predict the field in some frequency range at another point by assuming that the field pattern corotates with the sun.

Spatial inhomogeneities convected past the moon appear as temporal fluctuations of frequency

$$f = v_c/\lambda \qquad (1)$$

where $v_c \sim 400$ km/sec is the convection speed and λ is the spatial wavelength. We restrict our attention to spatial wavelengths much larger than the lunar diameter. This corresponds to frequencies $f << 10^{-1}$ Hz. It is then appropriate to treat the field changes seen by the moon as spatially uniform.

The power density spectrum of the interplanetary magnetic field is shown in Figure 1. The solid curve is taken from Siscoe et al. [1968], and the dashed curve is from Coleman [1968]. The dependence on frequency in the range shown is approximately $f^{-1.5}$ Hz. According to the analysis of Coleman, at frequencies above 2×10^{-5} Hz, the spectrum is dominated by fluctuations perpendicular to the theoretical spiral magnetic field direction. Below this frequency the spectrum is the result of fluctuations parallel to the spiral field direction, e.g., the corotation of the sector structure. This is the most energetic portion of the spectrum.

In a reference frame fixed with respect to the moon a motional field $\underline{E}_o = -\underline{V} \times \underline{B}_o$ exists in the solar wind. Additional time variations in the electric field are caused by fluctuations in the solar wind velocity, some of which are correlated with the sector structure [Wilcox, 1966]. The spectrum of the electric field is given by the convolution of the solar wind velocity spectrum with the spectrum of the perpendicular component of the interplanetary magnetic field.

The interpretation of surface magnetometer data requires a knowledge of the input spectra of the interplanetary magnetic and electric fields. This information can be provided by a magnetometer and plasma probe aboard a lunar orbiter, or, if it can be assured that the field pattern corotates with the sun (at the required frequencies), by an appropriate earth orbiting spacecraft. We shall hereafter assume that the input spectra are known.

3. ELECTRICAL CONDUCTIVITY OF THE MOON

The response of the moon to the magnetic and electric source fields is dependent upon its electrical properties. At the frequencies of interest here, the electrical conduction properties of rocks are adequately characterized by the DC conductivity, and conduction currents are typically much greater than displacement currents.

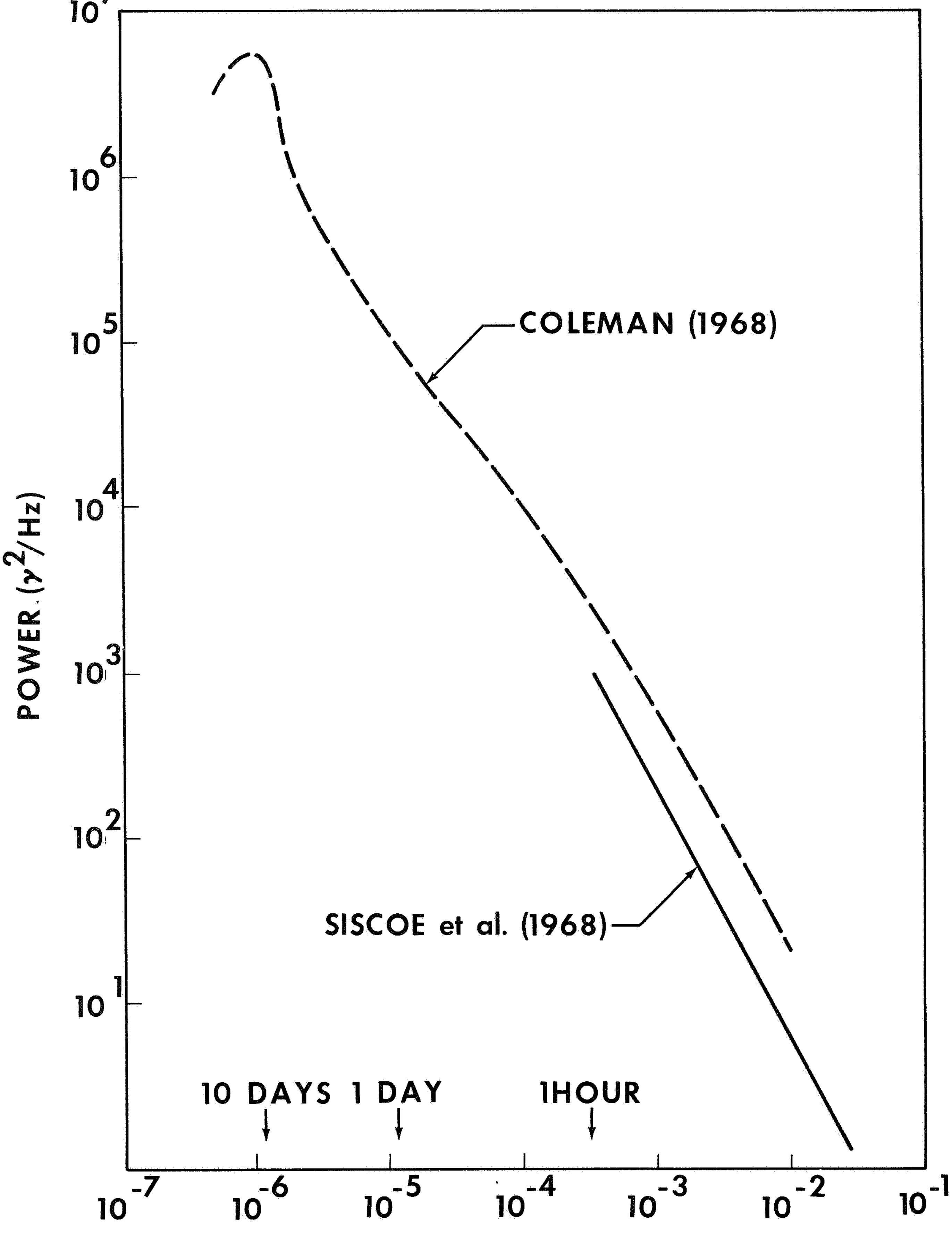

FIGURE 1 - POWER DENSITY SPECTRUM OF THE INTERPLANETARY MAGNETIC FIELD

As indicated above, the lack of a disturbance in the solar wind on the sunlit side of the moon is compatible with either a low conductivity lunar interior $\sigma < 10^{-5}$ $(\Omega m)^{-1}$ or a more conductive core surrounded by a resistive crust. In the latter case a layer 100 m to 1 km thick with $\sigma < 10^{-9}$ $(\Omega m)^{-1}$ or even a 10 m layer with $\sigma < 10^{-10}$ $(\Omega m)^{-1}$ will effectively limit the current and shield the conductive interior. These conductivities are to be compared with the conductivities of probable surface materials, i.e., dry rocks and volcanic ash, for which measurements have been reported in the range from $10^{-9}(\Omega m)^{-1}$ to $10^{-12}(\Omega m)^{-1}$ [Ward et al., 1968; Ward, 1969].

Present information on the conductivity of the lunar interior is based on theoretical studies. England et al. [1968] have calculated the electrical conductivity of the moon for various thermal models using the electrical properties of olivine. The two thermal models shown in Figure 2 are based on a young, 0.9 billion-year, and an old, 4.5 billion-year, chondritic moon.

The mineral composition of chondritic meteorites is predominately olivine (45%) and pyroxene (30%). At present no measurements of the electrical conductivity of chondrites are available. However, there are data on the electrical conductivity of olivine including the effects of pressure. The conductivity of the moon based on the two thermal models and the electrical properties of olivine is shown in Figure 3. These profiles are characterized by an inner region where the conductivity is an insensitive function of radius, surrounded by a region where σ decreases rapidly with increasing radius. We term the inner region the core, and the outer region the crust. For the young, cold moon, the maximum conductivity in the lunar interior is $10^{-2}(\Omega m)^{-1}$, and for the old, hot moon it is almost $10(\Omega m)^{-1}$. The dashed curve represents a hot moon with partial melting in the interior. The partial melting results in an increase in the maximum conductivity to nearly $10^{2}(\Omega m)^{-1}$. Thus, there is a 3 to 4 order of magnitude difference in the interior electrical conductivity between these cold and hot lunar models. While additional laboratory measurements of the temperature and pressure dependence of the conductivity of suspected lunar materials are desirable, it should be noted that the electrical properties of olivine predict a conductivity profile for the earth's mantle which is in reasonable agreement with experimental measurements [England et al., 1968].

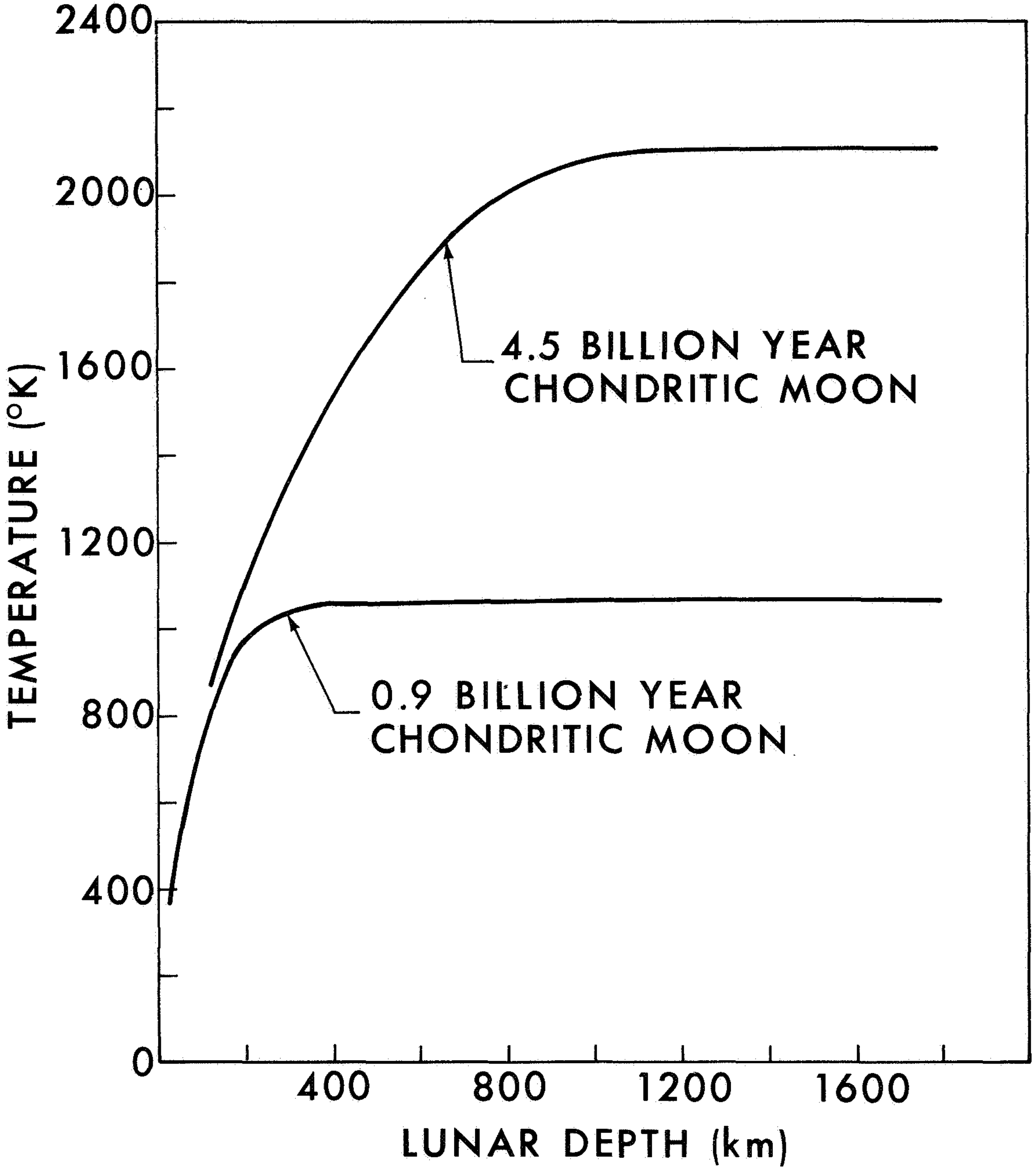

FIGURE 2 - LUNAR TEMPERATURE PROFILES, AFTER ENGLAND ET AL., (1968)

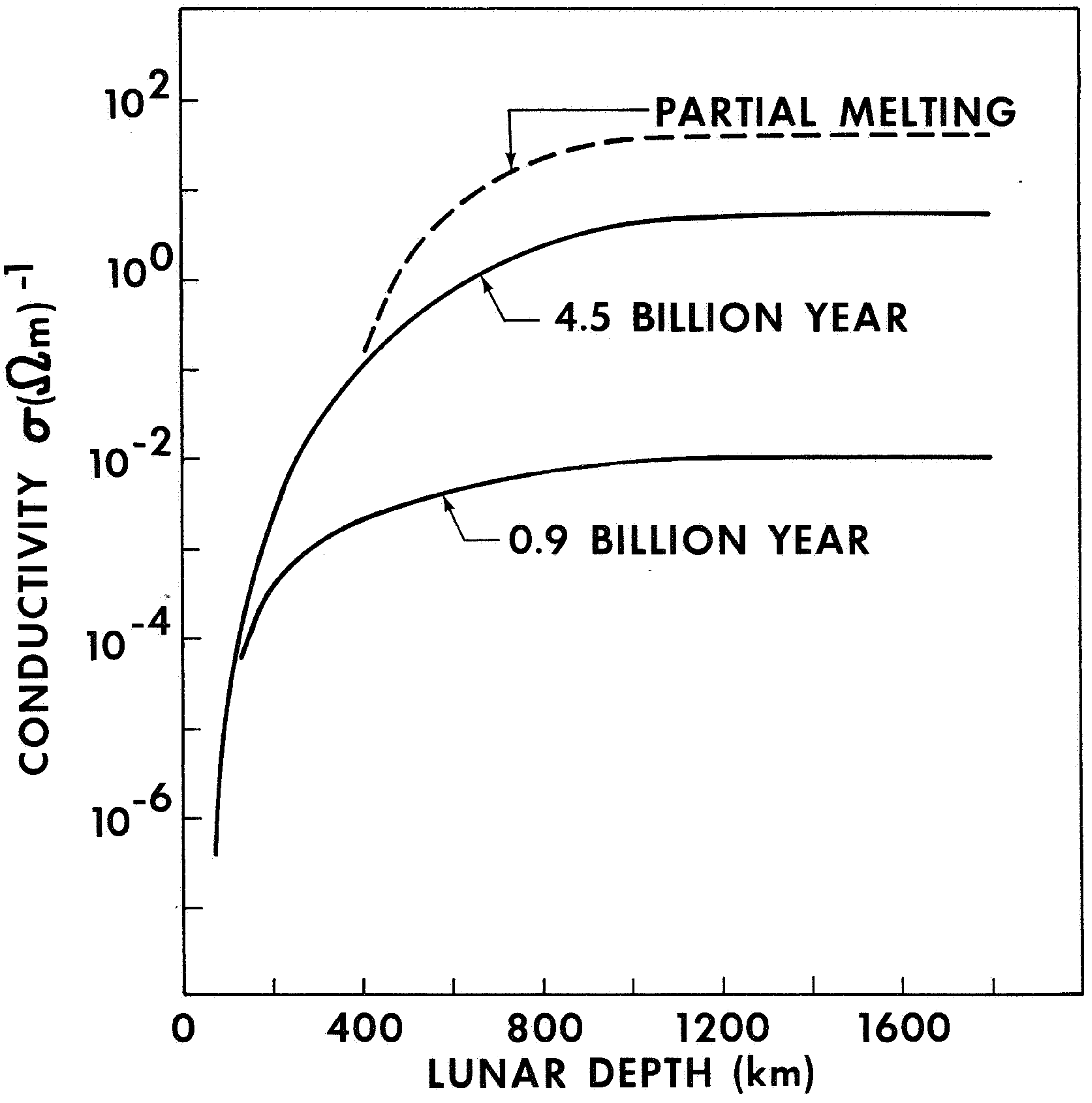

FIGURE 3 - LUNAR CONDUCTIVITY PROFILES, AFTER ENGLAND ET AL., (1968)

4. MULTI-LAYER MODELS

The foundation of the response model of Paper I rests on the energy density of any lunar magnetic field being much less than that of the streaming solar wind. It then follows that any lunar field is compressed and excluded from the oncoming solar wind by currents which flow in the conductive plasma environment adjacent to the sunlit lunar surface. It is further shown that this confining current exists in a sufficiently thin layer so that the actual volume current may be replaced by a surface current, whose magnitude is determined by the condition that only the unperturbed interplanetary magnetic field exists exterior to the model surface current. This provides a boundary condition at the sunlit lunar surface which permits the solution of Maxwell's equations in the lunar interior.

A two-layer, core-crust lunar electrical conductivity model is assumed in Paper I. This representation is entirely adequate to demonstrate the relevant physics of the interaction. However, to develop an understanding of the experimental limitations, it is instructive at this time to investigate the consequences of proceeding to multi-layer models. In principle, this allows a variable profile $\sigma(r)$ to be represented to any desired accuracy. Since the poloidal and toroidal response modes are orthogonal, the solutions for the magnetic source (poloidal) and the electric source (toroidal) can be solved for separately and then summed.

4a. Poloidal Magnetic Field

The geometry is shown in Figure 4. As presented in Paper I, the magnetic field at a frequency ω in the ith layer is

$$B_r = \frac{1}{k_i r} \sum_{n=1}^{\infty} n(n+1)\psi_{ni} \tag{2}$$

$$B_\theta = \frac{1}{k_i r} \sum_{n=0}^{\infty} \frac{\partial^2}{\partial r \partial \theta} (r\psi_{ni}) \tag{3}$$

$$\psi_{ni} = [\alpha_{ni} j_n(k_i r) + \beta_{ni} y_n(k_i r)] P_n(\cos\theta) \tag{4}$$

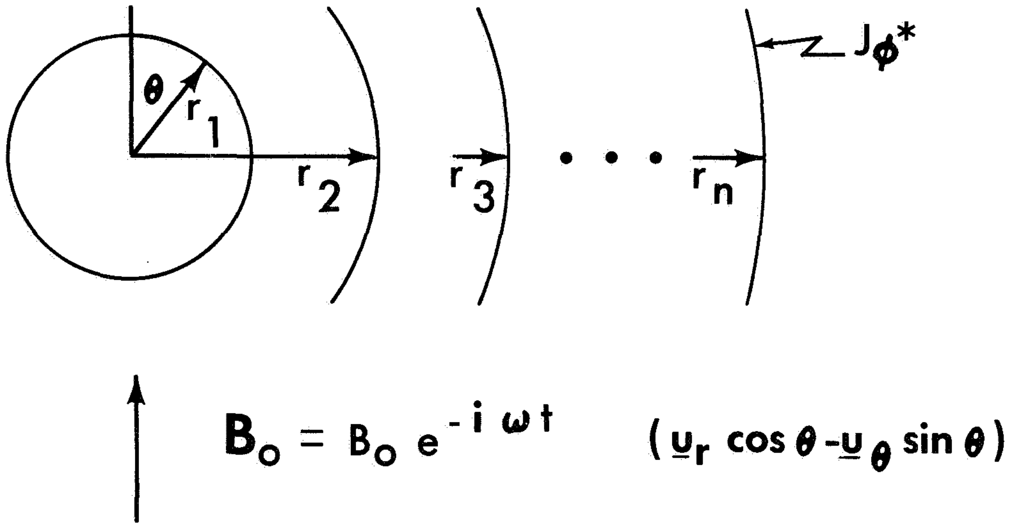

FIGURE 4 - GEOMETRY OF THE MULTI-LAYERED LUNAR MODEL, THE SURFACE CURRENT J* AND THE UNIFORM SOURCE FIELD B_o

where $j_n(z)$ and $y_n(z)$ are the spherical Bessel functions, $P_n(\cos\theta)$ the Legendre polynomials, and the time dependence $e^{-i\omega t}$ has been omitted. For a spatially uniform source field, only the n=1 terms remain in the sums (2) and (3), and the field in any layer reduces to (see equations 3-5 of Paper I)

$$b_i(r) = M_i(r)C_i, \qquad r_{i-1} \leq r \leq r_i \tag{5}$$

where

$$b_i(r) = \begin{bmatrix} B_r/B_o \cos\theta \\ \\ B_\theta/B_o \sin\theta \end{bmatrix} \tag{6}$$

is the normalized magnetic field vector, and

$$M_i = \frac{1}{k_i r} \begin{bmatrix} 2j_1(k_i r) & 2y_1(k_i r) \\ \\ j_1(k_i r) - k_i r\, j_o\,(k_i r) & y_1(k_i r) - k_i r\, y_o\,(k_i r) \end{bmatrix} \tag{7}$$

$$C_i = \begin{bmatrix} \alpha_{1i} \\ \\ \beta_{1i} \end{bmatrix} \tag{8}$$

and

$$k_i = \left[i\mu\sigma_i\omega + \varepsilon_i\mu\omega^2\right]^{1/2} \approx \left[i\mu\sigma_i\omega\right]^{1/2} \tag{9}$$

The boundary conditions are that b_i is finite at $r = 0$ and continuous everywhere except at the lunar surface, where we allow a jump, $\langle B_\theta \rangle = \mu J_\phi^*$ due to the model surface current J_ϕ^*. The use of this boundary condition is discussed in Paper I and in more detail by Blank and Sill [1969b]. In the undisturbed solar wind we have

$$b_{n+1} = \begin{bmatrix} 1 \\ \\ -1 \end{bmatrix} = \begin{bmatrix} 0 \\ \\ \mu J_\phi^*/B_o \sin\theta \end{bmatrix} + T \begin{bmatrix} \alpha_{11} \\ \\ 0 \end{bmatrix} \tag{10}$$

where

$$T = P_n P_{n-1} \cdot \cdot \cdot P_2 M_1 (r_1) \tag{11}$$

and P_i is the propagation matrix

$$P_i = M_i (r_i) M_i^{-1} (r_{i-1}) \tag{12}$$

From (10) we find

$$\alpha_{11} = 1/T(1,1)$$

$$\mu J_\phi^*/B_o \sin\theta = -[1+T(2,1)/T(1,1)] \tag{14}$$

Thus, the magnetic field at the lunar surface is

$$B_r = B_o \cos\theta \tag{15}$$

$$B_\theta = \frac{T(2,1)}{T(1,1)} B_o \sin\theta \tag{16}$$

The quantities B_o and θ specify the interplanetary field at the frequency ω and are assumed known. It is the transfer function

$$H_p(\omega) = \frac{B_\theta(\omega)}{B_o(\omega)\sin\theta} = \frac{T(2,1)}{T(1,1)} \tag{17}$$

which is a function of ω and the model parameters, that is to be derived from the surface magnetometer measurements.

4b. Toroidal Magnetic Field

In this mode the electric field is poloidal and we can adopt the formalism of the preceding section in the solution for the electric fields. The geometry is the same as in Figure 4 with $\underline{E}_o$ replacing $\underline{B}_o$. Since $\underline{E}_o$ and $\underline{B}_o$ are in reality not parallel, the coordinate systems for the poloidal and toroidal fields are rotated with respect to each other.

The usual boundary conditions at each layer interface require the continuity of the radial current density and the tangential electric field. At the surface the tangential field is equated to the tangential component of the source electric field. This surface boundary condition is equivalent to neglecting the resistance of the plasma relative to the resistance of the moon and is compatible with a weak interaction.

In each layer we have

$$e_i(r) = N_i(r)C_i, \qquad r_{i-1} \leq r \leq r_i \tag{18}$$

where

$$e_i(r) = \begin{bmatrix} \sigma_i\ E_r/E_o \cos\theta \\ \\ E_\theta/E_o \sin\theta \end{bmatrix} \tag{19}$$

is the normalized electric field vector and

$$N_i = \begin{bmatrix} \sigma_i M_i(1,1) & \sigma_i M_i(1,2) \\ M_i(2,1) & M_i(2,2) \end{bmatrix} \tag{20}$$

At the surface we have

$$e_n = \begin{bmatrix} J_r/E_o \cos\theta \\ -1 \end{bmatrix} = S \begin{bmatrix} \alpha_{11} \\ 0 \end{bmatrix} \tag{21}$$

where

$$S = Q_n\, Q_{n-1} \cdot \cdot \cdot\, Q_2 M_1(r_1) \tag{22}$$

$$Q_1 = N_i(r_i) N_i^{-1}\, (r_{i-1}) \tag{23}$$

From (21) we find

$$J_r = - \frac{S(1,1)}{S(2,1)} E_o \cos\theta \tag{24}$$

The surface magnetic field is then

$$B_\phi(r_n) = - \frac{\mu r_n}{2} \frac{S(1,1)}{S(2,1)} E_o \sin\theta \tag{25}$$

which gives the transfer function for this mode as

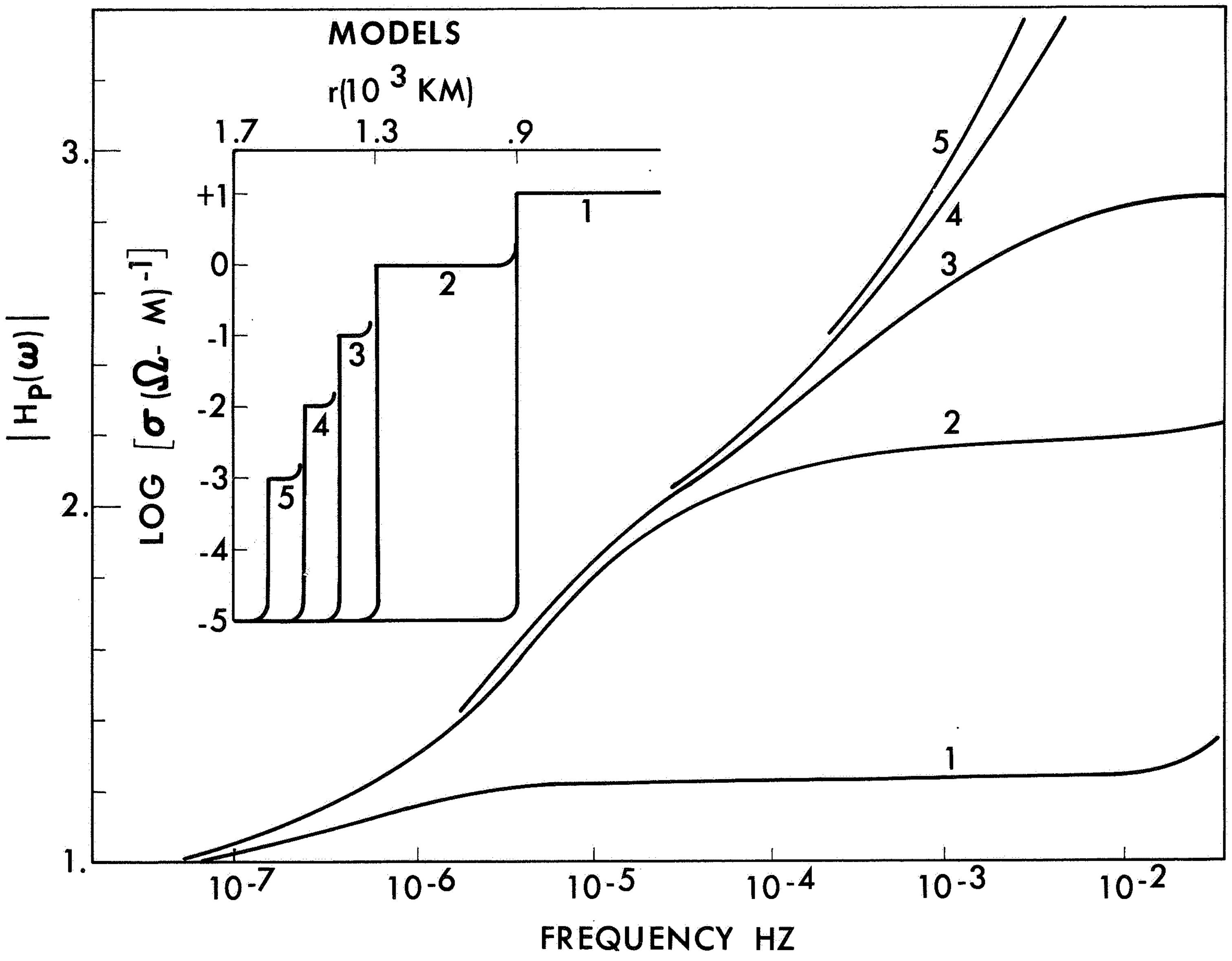

FIGURE 5 - MAGNITUDE OF THE POLOIDAL TRANSFER FUNCTION AS A FUNCTION OF FREQUENCY FOR 5 LUNAR MODELS ILLUSTRATING THE EFFECTS ON THE TRANSFER FUNCTION AS LAYERS ARE BUILT UP AROUND THE CORE

$$H_t(\omega) = \frac{B_\phi(\omega)}{B_{o\perp}(\omega)\sin\theta} = -\frac{\mu r_n}{2}\,\frac{S(1,1)}{S(2,1)}\,\frac{E_o(\omega)}{B_{o\perp}(\omega)} \tag{26}$$

Here, the spectrum of the electric field is given by the convolution of the solar wind velocity spectrum with the perpendicular component of the interplanetary magnetic field spectrum, i.e.,

$$E_o(\omega) = -V(\omega) * B_{o\perp}(\omega) \tag{27}$$

5. COMPUTATIONAL RESULTS

The lunar response for any conductivity model is represented by the transfer function which is the ratio of the output to the input spectra for the tangential components of the field. Figure 5 displays a family of curves which illustrate the effects on the poloidal transfer function as layers are built up around a core. The first curve is for a simple core-crust model. At very low frequencies the transfer function is equal to 1 and no secondary fields are induced. Induction in the core begins to be important at 10^{-7} Hz as is shown by the increase of the transfer function. At 10^{-5} Hz the response to the core is saturated and it is effectively behaving as a perfect conductor. The transfer function is then flat to 10^{-2} Hz where is begins to increase again due to induction in the crust. The results for this model are the same as those discussed in Paper I.

The addition of a third layer between the core and crust, as represented by model 2, produces two changes in the transfer function, namely an increase in its magnitude and a shift of the saturation region to higher frequencies. These effects are due to the induction in the middle layer. As additional layers are successively included to more closely approximate a continuous conductivity profile, the transfer function increases at the higher frequencies, i.e., induction in the outer, less conductive layers is important at successively higher frequencies.

To ascertain certain limitations involved in the interpretation of the transfer function in terms of a conductivity model, we compare the computed poloidal response for the two conductivity models shown in Figure 6. Model 5 has a smaller core of higher conductivity than model 6, and both are identical in the outer 200 km. Model 6 has a coarser conductivity structure in the interior which leads to a less smooth transfer

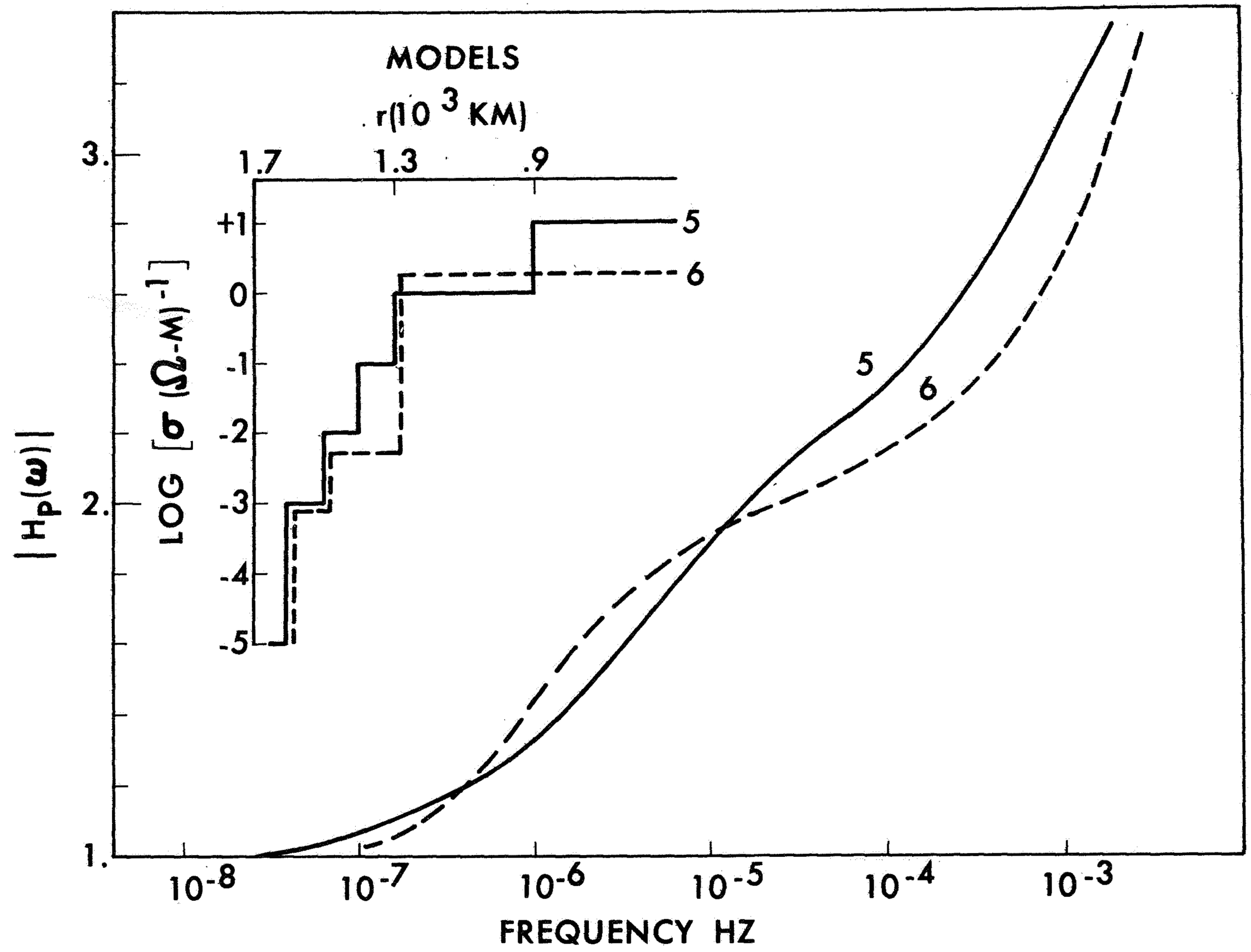

FIGURE 6 - MAGNITUDE OF THE POLOIDAL TRANSFER FUNCTION AS A FUNCTION OF FREQUENCY FOR TWO SIMILAR CONDUCTIVITY MODELS

function than that for model 5, but the two curves differ by less than 15%. This does not exceed plausible experimental and theoretical uncertainties associated with the determination of the transfer function. Therefore, it is unlikely that these two conductivity models could be discriminated.

Due to the three orders of magnitude difference between the interior conductivity in the hot and cold moons, the resolution difficulties between these models should not be too severe. For example, Figure 7 shows the poloidal transfer functions for hot and cold lunar models based on the conductivity profiles of England et al. [1968]. Here the transfer functions at any frequency differ by large factors, and discrimination between these two models should be unambiguous.

The toroidal transfer function for the hot model 5 is shown in Figure 8. Here and in subsequent calculations it is assumed that $-E_o/B_{o\perp} = V = 400$ km/sec. Note that the response is flat for frequencies less than 10^{-3} Hz, whereas the poloidal response for this model is frequency dependent in this region. In this model the current is limited by the DC resistance of the outer 100 km and induction effects in the inner layers are important only at very high frequencies (see Appendix and Blank and Sill [1969b]).

The dependence of the toroidal transfer function on the near surface conductivity structure is shown in the remaining curves of Figure 8. As the conductivity decreases in the surface layer, the strength of the response in the flat region decreases and the cut off region shifts to higher frequencies. The magnitude of the response in the flat region is given approximately by the DC expression for the motional generator for a two layer moon in which the resistance of the surface layer limits the current, i.e., $H_t = \mu_o V \sigma r^2/2z$, with $z<<r$ (radius of the moon) the thickness of the surface layer and σ its conductivity [Hollweg, 1968]. In model 5 the low frequency response is limited by the conductivity in the outer 100 km, in 5a by the average conductivity in the top 1 km. However, the value of the response for 5 and 5a is greater than 10 giving $B_\phi^2/2\mu_o > nmV^2$; therefore, these models are not compatible with the absence of a shock or strong interaction upstream from the moon.

Figure 9 shows the results for the toroidal transfer functions for a series of models (7a, 7b, 7c) with a conductivity structure below 100 km equal to that of the cold model 7, and in the outer 100 km a structure identical to that in models 5a,

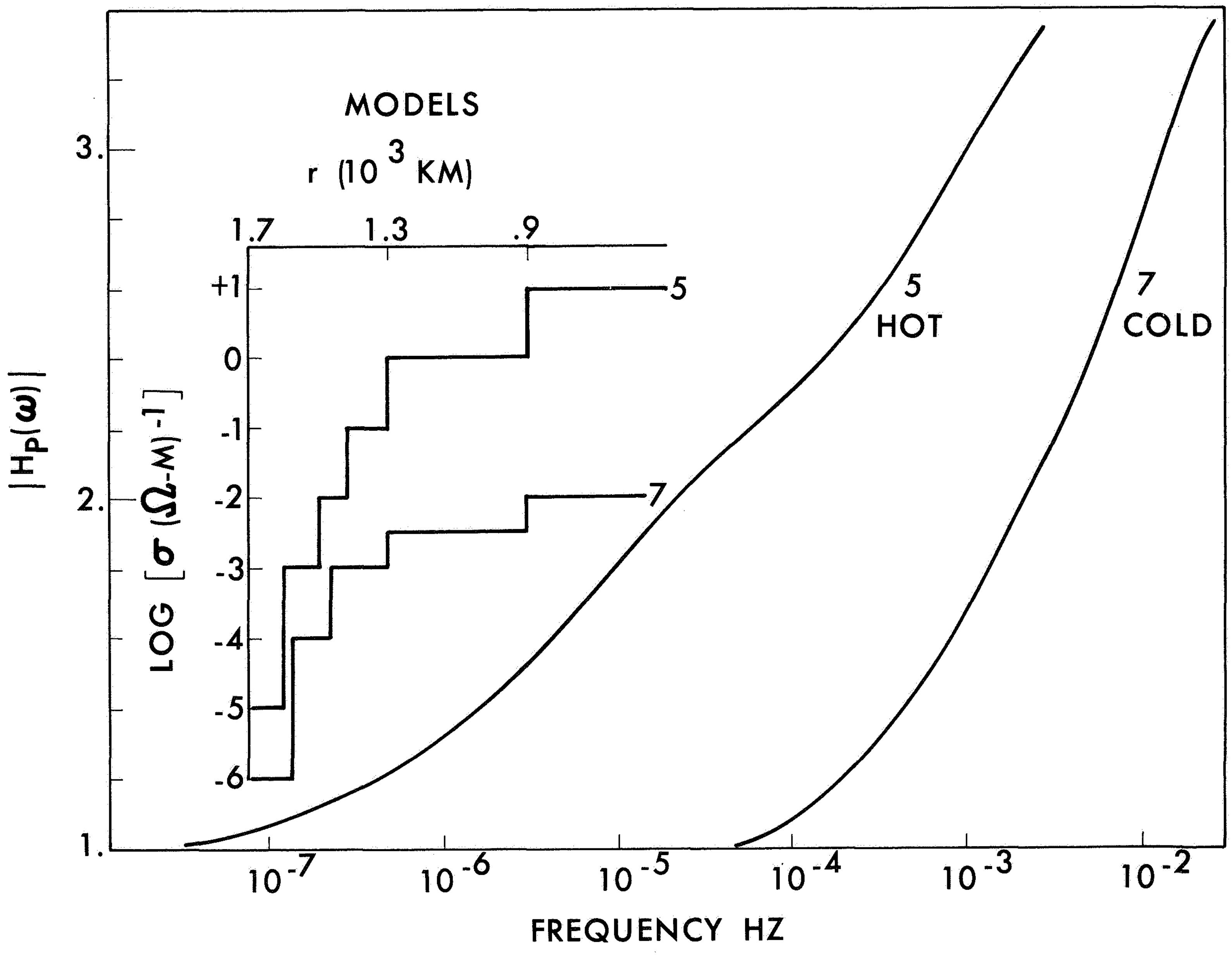

FIGURE 7 - MAGNITUDE OF THE POLOIDAL TRANSFER FUNCTION AS A FUNCTION OF FREQUENCY FOR HOT AND COLD LUNAR MODELS

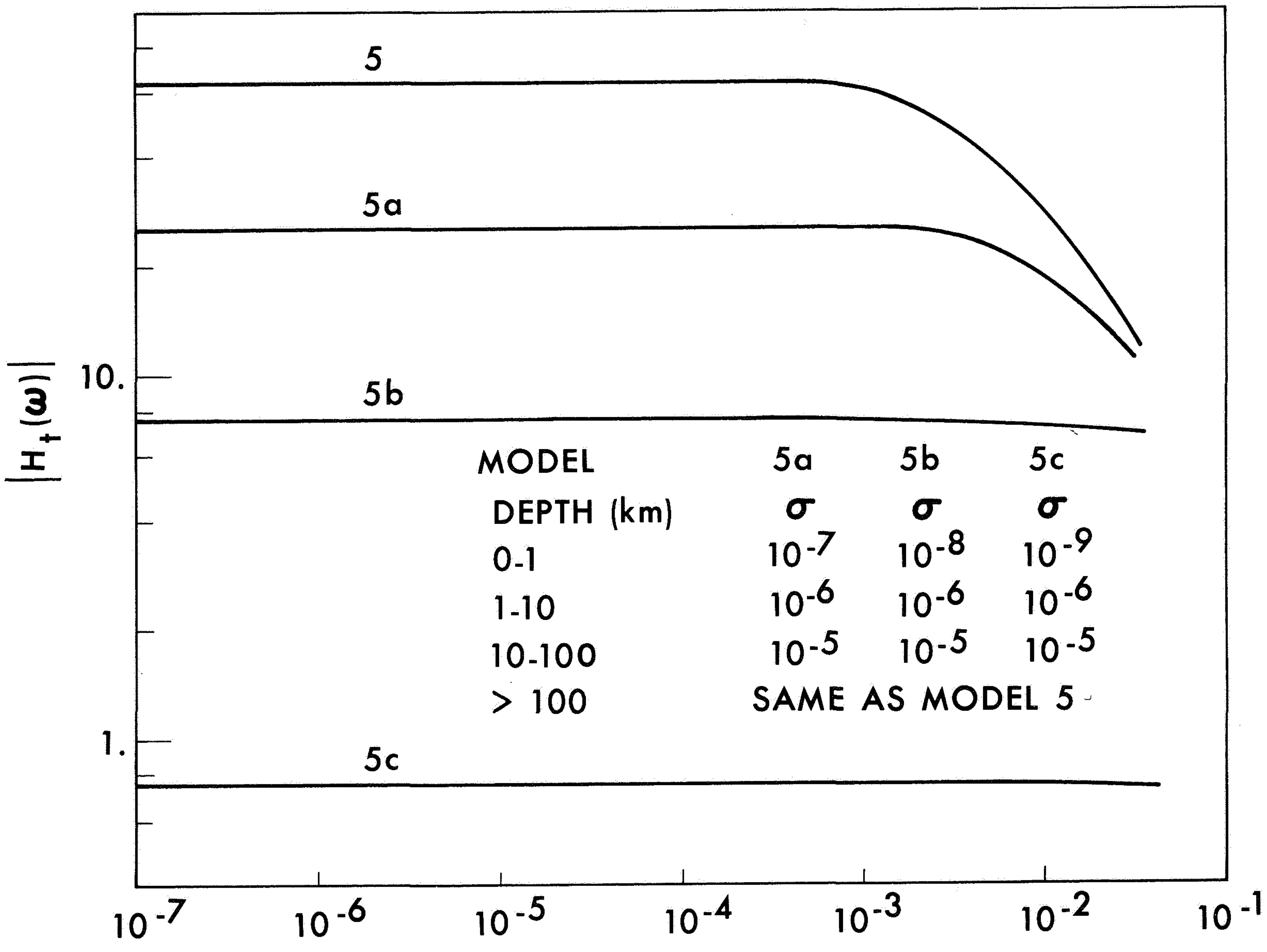

FIGURE 8 - MAGNITUDE OF THE TOROIDAL TRANSFER FUNCTION FOR HOT LUNAR MODELS

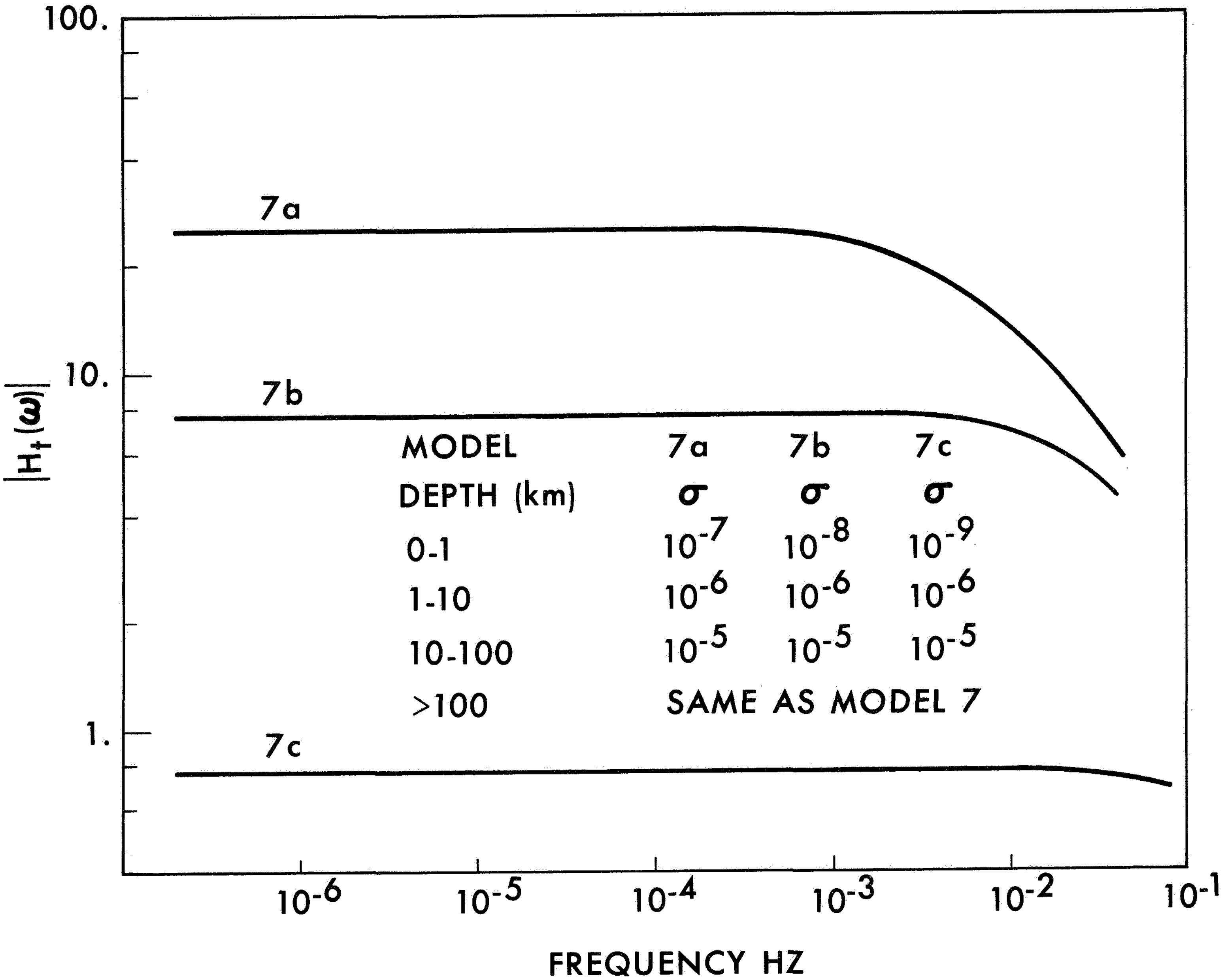

MODEL	7a	7b	7c
DEPTH (km)	σ	σ	σ
0-1	10^{-7}	10^{-8}	10^{-9}
1-10	10^{-6}	10^{-6}	10^{-6}
10-100	10^{-5}	10^{-5}	10^{-5}
>100	SAME AS MODEL 7		

FIGURE 9 - MAGNITUDE OF THE TOROIDAL TRANSFER FUNCTION FOR COLD LUNAR MODELS

5b and 5c. The transfer function in each case is almost identical to that of its counterparts 5a, 5b, or 5c. This is another illustration of the fact that the toroidal response depends almost exclusively on the near surface conductivity structure and cannot be used to distinguish between hot and cold models.

The transfer functions for several very cold lunar models with a maximum interior conductivity of $10^{-4}(\Omega m)^{-1}$ are presented in Figure 10. Both the poloidal and toroidal responses are flat below 10^{-3} Hz. At frequencies above 10^{-3} Hz the transfer functions are frequency dependent. However, the assumption of a uniform source field is no longer valid.

The examples presented here permit a separation of lunar conductivity models into two categories based on the magnitude of the interior conductivity. In the first category are those models with a relatively conductive interior, $\sigma \gtrsim 10^{-2}(\Omega m)^{-1}$. In this case the two responses are complimentary since, at frequencies which do not violate the assumption of a uniform source ($f<<10^{-1}$ Hz), the poloidal response is sensitive to the conductivity structure of the interior (depth >100 km) and the toroidal response is sensitive to the near surface (depth<100 km) conductivity structure. The frequency dependence of the poloidal response permits a "probing" of the interior electrical structure through skin depth effects. The toroidal response, in order to be compatible with the absence of a strong interaction, must be limited by the crustal resistance. The toroidal response is flat at frequencies much less than 10^{-1} Hz and is dependent only on the ratio σ/z, where σ is the conductivity of a surface layer of thickness z.

The second category includes those models with a poorly conductive interior, $\sigma<<10^{-2}(\Omega m)^{-1}$. For these models the poloidal response is flat for $f<<10^{-1}$ Hz and only an upper bound can be placed on the conductivity from measurements made of this response. The toroidal response for most reasonable models with an interior conductivity greater than $10^{-4}(\Omega m)^{-1}$, in order to be compatible with the absence of a shock, must be limited by the crustal resistance and therefore provides information on the near surface. However, the toroidal response may provide information on the interior conductivity if it is less than $10^{-5}(\Omega m)^{-1}$ and the current is not limited by the crustal resistance.

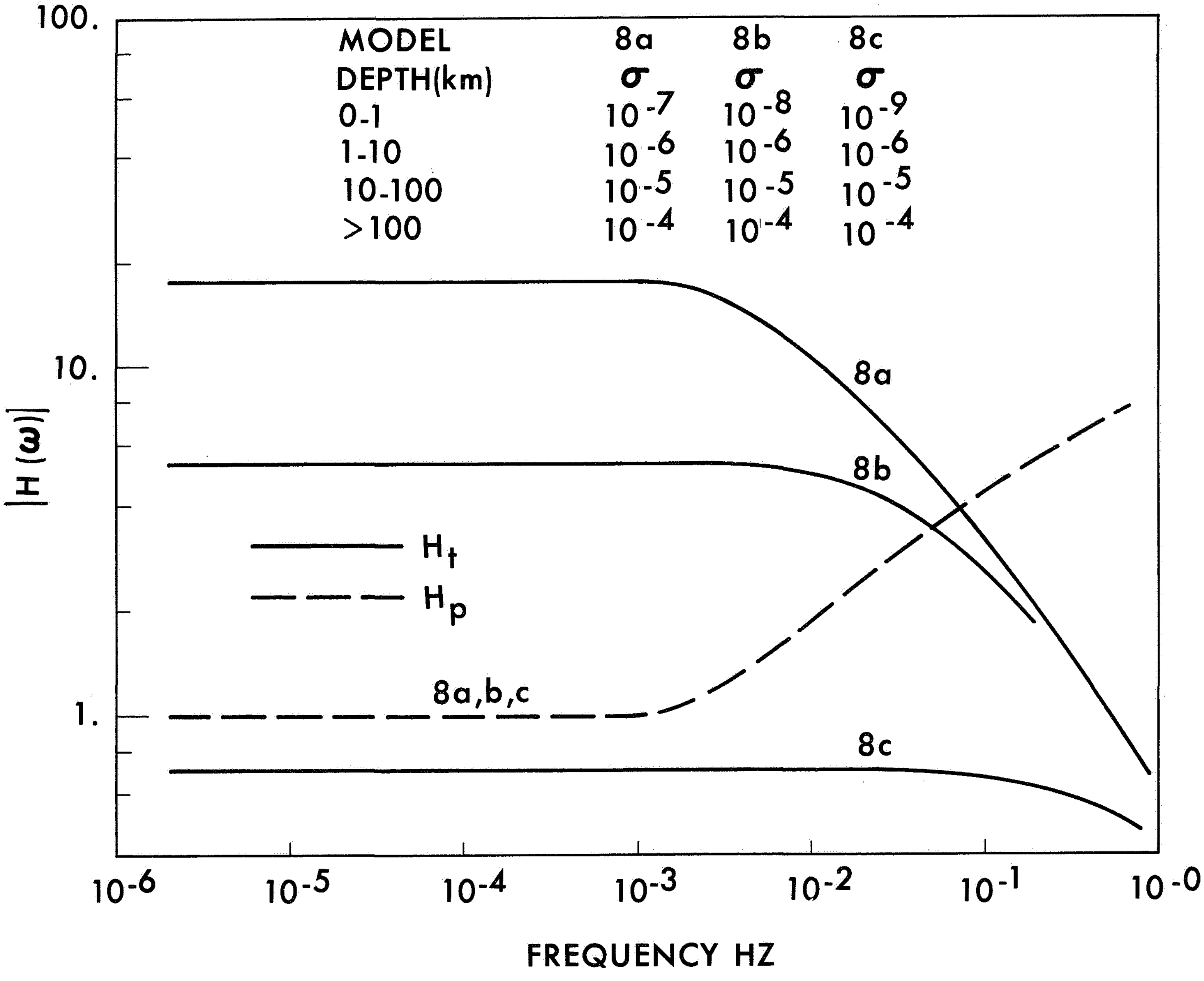

FIGURE 10 - MAGNITUDE OF THE TOROIDAL AND POLOIDAL TRANSFER FUNCTIONS FOR VERY COLD LUNAR MODELS

6. EXPERIMENTAL CONSIDERATIONS

Equations 15, 16 and 25 give the magnetic field in coordinate systems whose polar axes are in the direction of a Fourier component of the source field. Since the interplanetary source field orientation fluctuates, it is convenient to decompose the source fields into three orthogonal components in the solar ecliptic coordinates of Figure 11. In this coordinate system x and y are in the ecliptic plane, x points to the sun, SS is the subsolar point, and the z-axis passes through the north pole NP. Since the proposed Apollo landing sites are near equatorial, a local coordinate system (E-east, N-north, V-vertical) on the lunar equator is also shown. At an equatorial observation point located at an angle α from the subsolar point, the components of the field in the local coordinate system are

$$B_E(\omega) = H_p(\omega)\ [B_{ox}(\omega)\sin\alpha - B_{oy}(\omega)\cos\alpha] + H_t(\omega)B_{oy}(\omega) \tag{28}$$

$$B_N(\omega) = H_p(\omega)B_{oz}(\omega) - H_t(\omega)B_{oz}(\omega)\cos\alpha \tag{29}$$

$$B_V(\omega) = B_{ox}(\omega)\cos\alpha + B_{oy}(\omega)\sin\alpha \tag{30}$$

where

$$H_pB_{ox,y,z} = \frac{T(2,1)}{T(1,1)}\ B_{ox,y,z} \tag{31}$$

$$H_tB_{oy,z} = (-,+)\ \frac{\mu r}{2}\ \frac{S(1,1)}{S(2,1)}\ [V_{ox} * B_{oy,z}] \tag{32}$$

With measurements of the surface field spectrum provided by the ALSEP magnetometer, and simultaneous measurements of the source field spectra ($B_o(\omega)$, $V(\omega)$) by a spacecraft in the interplanetary medium, (28) and (29) can be solved for the two transfer functions $H_p(\omega)$, $H_t(\omega)$, and (30) can be used as a check on the model. The final step in the interpretation involves a comparison

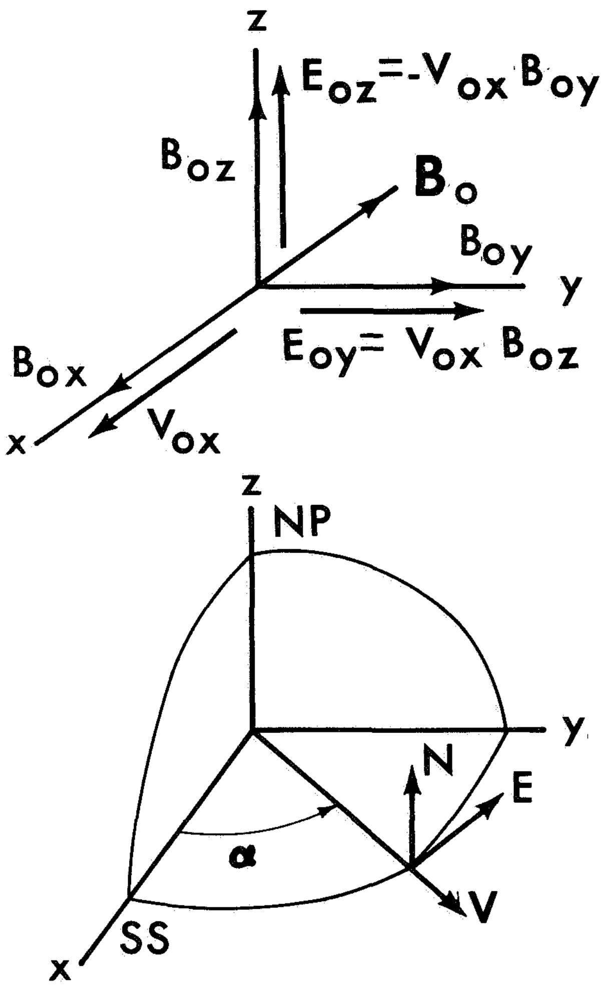

FIGURE 11 - THE INTERPLANETARY MAGNETIC FIELD AND A QUADRANT OF THE MOON IN A SOLAR ECLIPTIC COORDINATE SYSTEM. ALSO SHOWN IS THE LOCAL COORDINATE SYSTEM (E, N, V) IN WHICH THE LUNAR SURFACE FIELDS ARE MEASURED

of the observed transfer function with theoretical transfer functions calculated from proposed conductivity models as discussed in the previous section.

The above discussion of the interpretation of the data neglects certain effects caused by the rotation of the surface observation site with the moon. These effects are similar to those encountered in making magnetic field measurements from rotating satellites and are discussed by Sonett [1966]. The essence of the matter lies in the fact that the rotation of the observation point produces an amplitude modulation of the magnetic field. This is evident from the solution, (28) and (29), if we ascribe the effect of the rotation as producing the time dependence in the angle α, $\alpha = \Omega t$, where Ω is the angular rotation frequency of the moon. Alternatively, we can view this effect as resulting from the rotation of the source field at a frequency Ω measured with respect to a coordinate system fixed with the moon.

The modulation of the fluctuations in the time domain is equivalent to the convolution of the source spectrum $B_o(\omega)$ with the spectrum of the rotation $M(\omega)$. If our solutions (28) and (29) were exact over the entire lunar surface, then this simple sinusoidal amplitude modulation would give rise to a modulation spectrum $M(\omega)$ which consists of a pair of delta functions at $\omega = \underline{+}\Omega$, resulting in the replacement of $B_o(\omega)$ $(\sin \alpha, \cos \alpha)$ terms by terms like $B_o(\omega) * \delta(\omega \underline{+} \Omega)$. Inclusion of the effects of the day-night asymmetry or the effects of a nonuniform source field would require a spherical harmonic $[Y_{nm}(\theta,\phi)]$ expansion of the field in place of the Legendre polynomial $[P_n(\cos \theta)]$ representation given by (4). The effect of rotation which makes α function of time is then to introduce a modulation spectrum containing the harmonics of Ω.

The model we have chosen for the lunar interaction imposes certain restrictions on the frequencies which can be utilized to determine the transfer function. The high frequency limit is provided by the restriction that the source field be uniform with respect to the diameter of the moon, i.e., $f << 10^{-1}$ Hz. The low frequency limit arises due to the rotation of the moon about the earth. Figure 12 shows the moon in its orbit and the positions of the earth's magnetic tail and bow shock. The conditions for validity of our model require that measurements of the field be made on the sunlit hemisphere while the moon is in the solar wind or the transition region. A magnetometer placed at either point 1 or 2, which are 45° from the sub-earth point and at the east and west ends of the

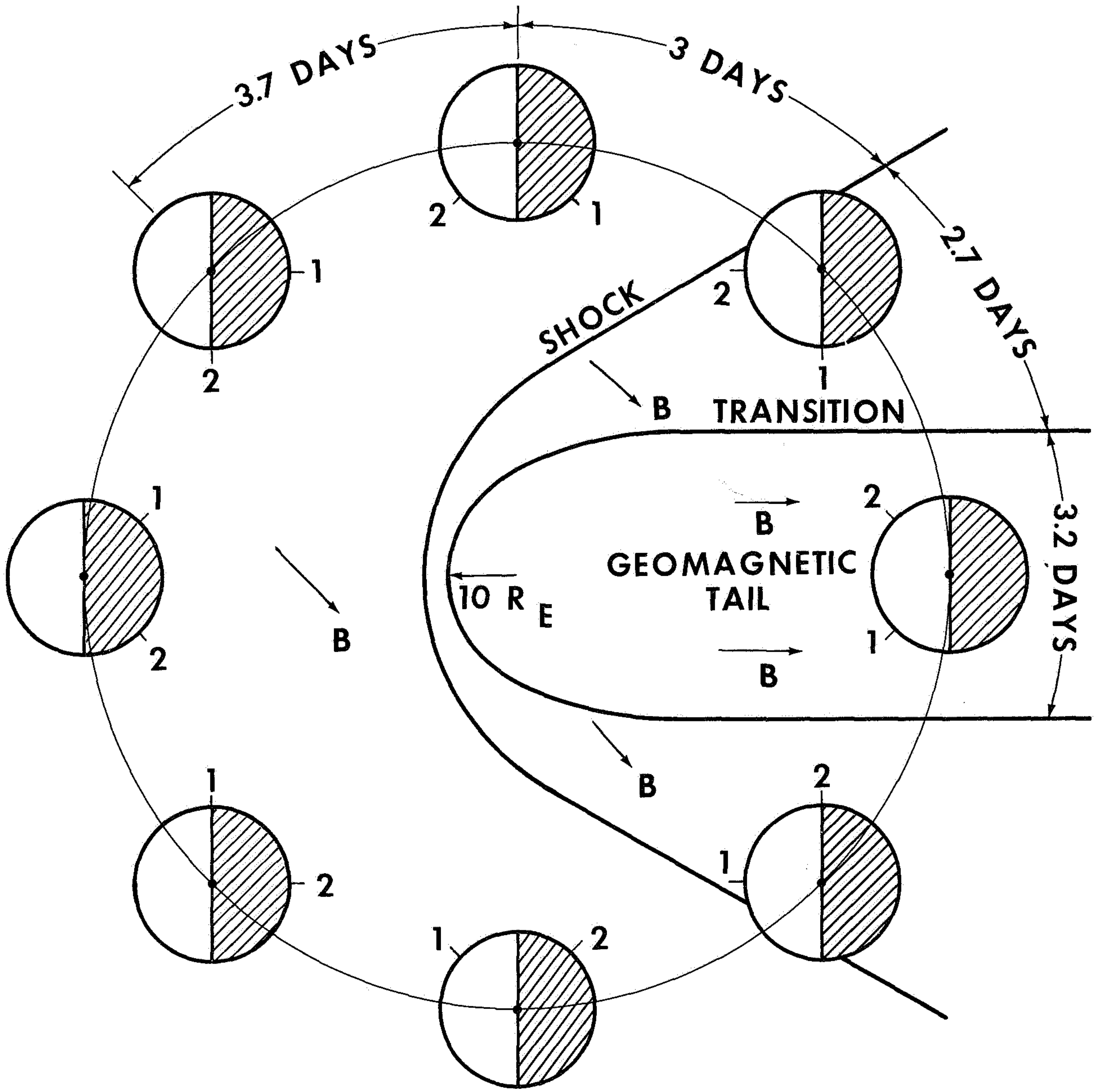

FIGURE 12 - ORBIT OF THE MOON, SHOWING THE EARTH'S BOW SHOCK AND THE GEOMAGNETIC TAIL

Apollo landing zone, would meet the above conditions for approximately 10 consecutive days during each lunation. The transformation of the 10 day time record into the frequency domain can be expected to provide information on the spectrum to frequencies as low as about 3×10^{-6} Hz ($\sim$3 day period).

From Figure 7 we see that the frequency range 3×10^{-6} to 10^{-3} Hz permits useful measurements of the poloidal transfer functions of both the hot and cold lunar models of England et al. In the above frequency range the cold model poloidal response is determined by the conductivity below 700 km depth ($r < 1000$ km) and thus the deep interior conductivity structure can be probed. In the same frequency range the hot model poloidal response is most sensitive to the conductivity structure at depths between 200 km and 800 km. At depths below 800 km ($r < 900$ km) the fields are effectively shielded and only a lower bound could be placed on the conductivity from measurements made in this frequency range. It is fortuitous that the frequency range determined by the restrictions of the experiment encompasses the region where the poloidal transfer functions for both hot and cold models are most sensitive to the deep electrical structure. If the actual lunar conductivity structure deviates significantly from the range given by these proposed models, for example Model 8, it will be necessary to extend one of the frequency limits if an estimate (other than a bound) of the interior conductivity is to be made. Extension of the low frequency limit requires a solution which includes the day-night asymmetry and, therefore, entails the use of the spherical harmonics Y_{nm}. In order to extend the high frequency limit to the region where the wavelength of the source field is of the order of the lunar radius, the more general scattering problem must be solved.

7. CONCLUSIONS

By interpreting the lunar response to fluctuations in the interplanetary electromagnetic field, an estimate of the lunar interior electrical conductivity may be obtained. Knowledge of the conductivity has certain implications regarding the thermal state of the lunar interior, and such information on the interior temperature is central to theories of lunar formation and history.

The suggested procedure is to obtain simultaneous measurements of the lunar surface magnetic field and the ambient, undisturbed interplanetary field and solar wind velocity. The spectral measurements permit the calculation of the transfer functions of the moon and, in addition, provide for a check on the theory of Paper I.

The theoretical model and experimental restrictions impose a frequency range $3 \times 10^{-6} \lesssim f \lesssim 10^{-3}$ Hz on the experiment. This range encompasses part of the most energetic portion of the source field spectrum and permits the probing of the deep electrical structure of currently proposed lunar conductivity models. The compatibility of any lunar conductivity (and associated thermal) model with the data can thus be ascertained. The resolution of the experiment should be sufficient to distinguish between lunar models based on different thermal histories.

W. R. Sill
W. R. Sill
J. L. Blank
J. L. Blank

1014-$^{\text{WRS}}_{\text{JLB}}$-jnr

Attachment
Appendix

REFERENCES

Blank, J. L., and W. R. Sill, Response of the moon to the time-varying interplanetary magnetic field, J. Geophys. Res., 74, 736-743, 1969a.

Blank, J. L., and W. R. Sill, Reply, J. Geophys. Res., 74, in press, 1969b.

Coleman, P. J., Jr., Turbulence, viscosity, and dissipation in the solar-wind plasma, Astrophys J., 153, 371-388, 1968.

England, A. W., G. Simmons, and D. Strangway, Electrical conductivity of the moon, J. Geophys. Res., 73, 3219-3226, 1968.

Hollweg, J. V., Interaction of the solar wind with the moon and formation of a lunar limb shock wave, J. Geophys. Res., 73, 7269-7276, 1968.

Ness, N. F., Simultaneous measurements of the interplanetary magnetic field, J. Geophys. Res., 71, 3319-3324, 1966.

Ness, N. F., Electrical conductivity of the moon (abstract), Trans. Am. Geophys. Union, 50, 216, 1969a.

Ness, N. F., The electrical conductivity and internal temperature of the moon, NASA-GSFC Report X-616-69-191, 1969b.

Sill, W. R., and J. L. Blank, Lunar response to the time-varying interplanetary magnetic field and application to the ALSEP magnetometer experiment, Bellcomm Technical Report TR-68-710-7, 1968.

Siscoe, G. L., L. Davis, Jr., P. J. Coleman, Jr., E. J. Smith, and D. E. Jones, Power spectra and discontinuities of the interplanetary magnetic field: Mariner 4, J. Geophys. Res., 73, 61-82, 1968.

Sonett, C. P., Modulation and sampling of hydromagnetic radiation, Space. Res., 6, 280-322, 1966.

Sonett, C. P., and D. S. Colburn, Establishment of a lunar unipolar generator and associated shock and wake by the solar wind, Nature, 216, 340-343, 1967.

Ward, S. H., Gross estimates of the conductivity, dielectric constant, and magnetic permeability distributions in the moon, Radio Sci., 4, 117-137, 1969.

References

Ward, S. H., G. R. Jiracek, and W. I. Linlor, Electromagnetic reflection from a plane-layered lunar model, J. Geophys. Res., 73, 1355-1372, 1968.

Wilcox, J. M., Solar and interplanetary magnetic fields, Science, 152, 161-166, 1966.

APPENDIX (contd.)

The response of a core-crust model for which the crust is thin ($z = r_2 - r_1 << r_2$) and non-inductive ($k_2 z << 1$) is

$$H_t = -\mu_o \frac{\sigma_2 r_2}{2} \frac{E_o}{B_o} \frac{\left[\frac{\sigma_1}{\sigma_2} (1 - \frac{2z}{r_2}) (1-R) + \frac{2z}{r_2} (1+R/2)\right]}{\left[\frac{\sigma_1}{\sigma_2} \frac{z}{r_2} (1-R) + (1 - \frac{z}{r_2}) (1+R/2)\right]} \qquad \text{(A-5)}$$

In the low frequency limit ($|k_1 r| << 1$), $R \rightarrow 0$ and (A-5) yields the expression for a two layer, DC motional generator derived by Hollweg [1968].

For those models in which the crust resistance is greater than the core resistance ($\sigma_1 z/\sigma_2 r_2 >> 1$) we find that the high frequency response is flat and equal to the DC response as long as $\sigma_1 z\ \delta_1/\sigma_2 r_2^2 >> 1$, i.e.,

$$H_t = -\mu_o \frac{\sigma_2 r_2}{2} \frac{E_o}{B_o} \frac{r_2}{z} \qquad \text{(A-6)}$$

for frequencies satisfying the condition

$$f << \left(\frac{\sigma_1 z}{\sigma_2 r_2}\right)^2 \frac{1}{\pi \mu_o \sigma_1 r_1^2} \qquad \text{(A-7)}$$

This condition indicates that as the conductivity ratio σ_1/σ_2 increases, the flat portion of the response is shifted to higher frequencies. The transfer function for the class of models in which the crust limits the current flow is then flat even in the frequency range where induction is becoming important in the core.

APPENDIX

TOROIDAL TRANSFER FUNCTIONS FOR SIMPLE MODELS

The toroidal transfer function for a homogeneous sphere is easily derived from (22), (18) and (7) to be

$$H_t = \frac{(1-R)}{(1+R/2)} \mu_o \frac{r_1 \sigma_1 E_o}{2B_o} \tag{A-1}$$

where

$$R = 1 - 3j_1(k_1 r_1)/k_1 r_1 j_o(k_1 r) \tag{A-2}$$

In the low frequency limit ($|k_1 r_1| << 1$), $R \rightarrow 0$ and we find that (A-1) reduces to the expression for the DC motional generator, i.e.,

$$H_t = -\mu_o \frac{r_1 \sigma_1}{2} \frac{E_o}{B_o} \tag{A-3}$$

At high frequencies ($|k_1 r_1| >> 1$), $R \cong 1 - 3\delta_1(1+i)/2r_1$ and we find that

$$H_t = -\mu_o \frac{\sigma_1}{2} \frac{E_o}{B_o} \delta_1(1+i) \tag{A-4}$$

where $\delta_1 = \sqrt{2/\mu\sigma_1\omega}$ is the skin depth. The decrease in the response at frequencies where induction is important is simply due to the exponential decay $\exp[-(r_1-r)/\delta_1]$ of the electric fields within the sphere.

DISTRIBUTION LIST

NASA Headquarters
R. J. Allenby/MAL
W. O. Armstrong/MTX
P. E. Culbertson/MLA
R. J. Green/MAL
E. W. Hall/MTG
D. P. Hearth/SL
T. A. Keegan/MA
R. L. Lohman/MTYY
M. A. Mitz/SL
W. T. O'Bryant/MAL
D. G. Rea/SL
A. W. Schardt/SG
L. R. Scherer/MAL
A. D. Schnyer/MTV
J. W. Wild/MTE
Nasa Headquarters
Library-USS-10

Ames Research Center
D. S. Colburn/SSE
P. Dyal/SSE
W. I. Linlor/SSE
L. Roberts/M (2)
C. P. Sonett/SS (3)
J. R. Spreiter/SST

Goddard Space Flight Center
J. E. Ainsworth/621
S. J. Bauer/615
R. E. Hartle/615
J. P. Heppner
G. D. Mead/641
N. F. Ness/612
C. C. Stephanides/620
D. A. Stern/641
R. G. Stone/615
W. F. Templemon/252
D. J. Williams/611

Jet Propulsion Laboratory
E. J. Smith/328
C. W. Snyder/32

Manned Spacecraft Center
W. N. Hess/TA
C. R. Hicks/FA4
J. L. Modisette/TG4

American Nucleonics Corporation
K. Schwartz

Cornell University
T. Gold

Environmental Science
Service Administration
J. R. Wait

Max-Planck Institut für
Extraterrestrische Physik
J. V. Hollweg

Massachusetts Institute
of Technology
J. H. Binsack
H. S. Bridge
E. F. Lyon
T. R. Madden
F. Press
G. Simmons
G. S. Siscoe

National Radio Astronomy
Observatory
J. W. Findlay

Princeton University
R. A. Phinney

Rice University, Houston, Texas
A. J. Dessler
F. C. Michael

Southwest Center for
Advanced Studies
F. S. Johnson/DASS
J. E. Midgley

DISTRIBUTION LIST (Continued)

United States Geological Survey - Flagstaff
R. E. Eggleton
H. Masursky
R. Regan
D. S. Roddy

The University, Newcastle-upon-Tyne, England
S. K. Runcorn

California Institute of Technology
L. Davis, Jr.
B. C. Murray
E. Shoemaker

University of Alaska
S. I. Akasofu
S. Chapman

University of California at Berkeley
K. A. Anderson
F. S. Mozer
S. Ward

University of California at Los Angeles
P. J. Coleman, Jr.
G. Schubert

University of California at San Diego
J. Arnold
H. Urey

University of Iowa
J. A. Van Allen

University of Kansas
D. B. Beard
W. W. Shen

University of New Hampshire
L. J. Cahill

Bellcomm, Inc.
G. M. Anderson
G. C. Bill
A. P. Boysen, Jr.
G. K. Chang
C. L. Davis
D. A. De Graaf
F. El-Baz
A. F. H. Goetz
D. R. Hagner
C. M. Harrison
J. W. Head
P. J. Hickson
N. W. Hinners
B. T. Howard
D. B. James
J. Kranton
M. Liwshitz
H. S. London
K. E. Martersteck
R. K. McFarland
J. Z. Menard
G. T. Orrok
W. L. Piotrowski
I. M. Ross
F. N. Schmidt
R. V. Sperry
C. M. Thomas
W. B. Thompson
J. W. Timko
R. L. Wagner
J. E. Waldo
M. P. Wilson
M. T. Yates
All members, Division 101
Central Files
Department 1024 File
Library


BELL
SYSTEM